

Formation, disruption and energy output of Population III X-ray binaries

Taeho Ryu^{1*}, Takamitsu L. Tanaka^{1,2}, Rosalba Perna^{1,3}

¹ *Department of Physics and Astronomy, Stony Brook University, Stony Brook, NY 11794-3800, USA*

² *Department of Physics, New York University, 4 Washington Place, New York, NY 10003, USA*

³ *Adjunct Fellow of JILA, 440 UCB, Boulder, CO 80309-0440, USA*

17 May 2018

ABSTRACT

The first astrophysical objects shaped the cosmic environment by reionizing and heating the intergalactic medium (IGM). In particular, X-rays are very efficient at heating the IGM before it became completely ionized, an effect that can be measured through the redshifted 21 cm line of neutral hydrogen. High-mass X-ray binaries (HMXBs), known to be prolific X-ray sources in star-forming galaxies at lower redshifts, are prime candidates for driving the thermal evolution of the IGM at redshifts $z \gtrsim 20$. Despite their importance, the formation efficiency of HMXBs from the first stellar populations is not well understood—as such, their collective X-ray emission and the subsequent imprint on the 21 cm signature are usually evaluated using free parameters. Using N -body simulations, we estimate the rate of HMXB formation via mutual gravitational interactions of nascent, small groups of the first stars (Population III stars). We run two sets of calculations: one in which stars form in small groups of five in nearly Keplerian initial orbits, and another in which two such groups collide (an expected outcome of mergers of host protogalaxies). We find that HMXBs form at a rate of one per $\gtrsim 10^4 M_\odot$ in newly born stars, and that they emit with a power of $\sim 10^{41}$ erg s^{−1} in the 2 – 10 keV band per solar mass per year of star formation. This value is a factor $\sim 10^2$ larger than what is observed in star forming galaxies at lower redshifts; the X-ray production from early HMXBs would have been even more copious, if they also formed *in situ* or via migration in protostellar disks. Combining our results with earlier studies suggests that early HMXBs were highly effective at heating the IGM and leaving a strong 21 cm signature. We discuss broader implications of our results, such as the rate of long gamma-ray bursts from Population III stars and the direct collapse channel for massive black hole formation.

Key words: cosmology: theory – early universe – cosmology: dark ages, reionization, first stars – stars: Population III – intergalactic medium – X-rays: binaries – stars: kinematics and dynamics

1 INTRODUCTION

A major outstanding goal in cosmology is to piece together the history of the Universe between Cosmic Dawn, the emergence of the first stars and galaxies, and the end of reionization, when the radiation from these objects had ionized the intergalactic medium (IGM). Advances in numerical techniques, combined with exquisite measurements of the “initial” conditions (at a redshift $z \approx 1000$; Hinshaw et al. 2013, Planck Collaboration et al. 2015), have led to remarkable simulations (e.g. Abel, Bryan & Norman 2002; Turk, Abel & O’Shea 2009; Stacy, Greif & Bromm 2010; Greif et al. 2011;

Bromm & Yoshida 2011) of the conditions leading up to the former milestone, occurring at $z \gtrsim 30$, when the Universe was ≈ 100 Myr old. However, reconstructing the subsequent several hundred Myr of cosmic history has proved far more challenging, due to the difficulties in reliably modeling the numerous forms of feedback from the first astrophysical objects (e.g. Springel, Di Matteo & Hernquist 2005; Stinson et al. 2006; Sijacki et al. 2007).

In particular, X-rays from the first galaxies can act as a powerful source of feedback (e.g. Venkatesan, Giroux & Shull 2001; Machacek, Bryan & Abel 2003) that exerts influence over a wide range of distance scales. Because hard X-rays (energies $\gtrsim 1$ keV) have mean free paths comparable to the Hubble horizon, they can isotropically heat and

* email: taeho.ryu@stonybrook.edu

partially reionize the early IGM (e.g. Oh 2001; Venkatesan, Tumlinson & Shull 2003; Ricotti & Ostriker 2004; Pritchard & Furlanetto 2007). In fact, they are expected to be the dominant agent in heating the IGM. Such heating may suppress star formation (Ripamonti, Mapelli & Zaroubi 2008) and massive black hole (BH) growth (Tanaka, Perna & Haiman 2012) inside low-mass dark matter haloes by raising the Jeans and filtering masses of the IGM (Gnedin 2000; Naoz & Barkana 2007). On galactic and circum-galactic scales, soft X-rays ($\sim 0.1 - 1$ keV) can affect the formation of stars and possibly massive black holes (BHs) by promoting the formation of molecular hydrogen via electron-catalyzed reactions (e.g. Haiman, Rees & Loeb 1996; Kuhlen & Madau 2005; Latif et al. 2015; Inayoshi & Tanaka 2015).

In addition to their suspected roles in early galaxy evolution, X-rays are important also because they can leave an observable signature that can be exploited to probe the cosmological epoch in question (Pritchard & Loeb 2008). Their thermal impact on the early Universe should be measurable through the redshifted 21 cm transition line of neutral hydrogen, which is observed in emission or absorption depending on the relative temperature of the IGM with respect to that of the cosmic microwave background (CMB). Several studies have investigated how forthcoming observations of the sky-average amplitude and power spectrum of the relic 21 cm line (e.g. Bowman, Rogers & Hewitt 2008; Burns et al. 2012; van Haarlem et al. 2013; Voytek et al. 2014) could be used to constrain the astrophysical agent (or agents) responsible for heating the early IGM.

There are sound reasons to expect that the first galaxies produced X-rays in abundance, and rapidly heated the IGM. There are two dominant X-ray sources in present-day galaxies—both powered by gas accretion onto BHs, and both plausibly prominent shortly after Cosmic Dawn: gas feeding massive BHs shining as active galactic nuclei (AGN), and X-ray binaries, powered by a stellar-mass BH gradually cannibalizing a companion star. Estimates of the mass accumulated by nuclear BHs prior to $z \sim 6$ (Shankar, Weinberg & Miralda-Escudé 2009; Salvaterra et al. 2012a), the existence of very massive BHs at $z \gtrsim 6$ (e.g. Fan et al. 2001; McGreer et al. 2006; Willott et al. 2007, 2009; Mortlock et al. 2011; Venemans et al. 2013; Bañados et al. 2014), as well as the observed (e.g. Shen et al. 2007) and theoretically expected (Shankar, Weinberg & Miralda-Escudé 2009; Tanaka 2014) increase in their duty cycles toward higher redshifts, all hint that X-ray AGN may have been much more common during this epoch. Likewise, high-mass X-ray binaries (HMXBs) dominate the X-ray emission of star-forming galaxies; the low metallicity and rapid baryonic mass accretion of the earliest galaxies both lend credence to the notion that they were rife with HMXBs. Theoretical models suggest that either type of X-ray source could heat the IGM to above the CMB temperature as early as $z \sim 30$, and that this transition should be measurable by the planned 21 cm experiments.

At present, there are too many theoretical uncertainties to determine from the future data which type of X-ray source—AGN or HMXBs—was responsible for driving the thermal evolution of the $z \lesssim 30$ IGM. Modeling the early AGN X-ray emission is particularly difficult, because the conditions for triggering AGN activity are not fully understood even at low redshifts (e.g. Hopkins & Quataert

2010; Treister et al. 2012); because of the uncertainty in the fraction of X-ray photons that is released into the IGM as opposed to being trapped inside the accretion flow or reprocessed into the infrared (e.g. Madau, Haardt & Dotti 2014; Pacucci et al. 2015); and because the epoch, initial masses, and birthplaces of the massive BH “seeds” are not yet constrained by observations (e.g. Volonteri 2010; Haiman 2013; Tanaka & Li 2014). Similarly, studies usually estimate the X-ray contribution from early HMXBs by simply inferring empirical relations between X-ray luminosity and star formation rate (SFR) in local galaxies (and modeling the SFR using a semi-analytic cosmological model), or combining such relations with one or more free parameters (e.g. Mirabel et al. 2011; Tanaka, O’Leary & Perna 2015).

The goal of this study is to alleviate the uncertainties in the formation rate and X-ray output of HMXBs in the early Universe, by using N -body simulations of nascent groups of the first (Population III, henceforth Pop III) stars. We choose the properties of the star groups in our simulations to reflect those found in hydrodynamical simulations of Pop III star formation at $z \sim 20$ (Greif et al. 2012, Stacy & Bromm 2013). We follow the formation and dynamical evolution of compact binaries over thousands to millions of years, including the effects of the background gravitational potential and dynamical friction. This allows us to compute the fraction of Pop III stars that form stable, compact binaries, and eventually undergo an X-ray bright phase. The end result is an estimate of the formation rate of HMXBs in the first protogalaxies, as well as the amount of X-rays they generate per unit star formation. To our knowledge, this is the first published estimate of this type.

Our simulations predict a binary formation rate which is similar to what is observationally inferred in present-day galaxies. However, we derive a HMXB energy output (normalized to the star formation rate) that is a factor $\sim 10 - 150$ higher than in present-day star-forming galaxies, if the HMXB duty cycle is similar to the one in the local Universe. We find that the X-ray output does not change significantly within the wide variety of simulation setups considered—such as different orientations for collisions between star groups, and ambient gas density—and submit that this is a robust estimate.

The findings of this study can be used as model inputs in estimating the 21 cm global signature and power spectrum, but have wider applications. As stated above, the X-ray output of the first galaxies are also of interest for studying feedback on smaller scales, such as subsequent star formation and massive BH formation.

Our work is also relevant for predicting the rates of long-duration gamma-ray bursts (LGRBs) from Pop III stars. LGRBs are important probes that can shed light on the Universe out to $z > 10$ (e.g. Toma, Sakamoto & Mészáros 2011). According to the collapsar model (MacFadyen & Woosley 1999), progenitors of LGRBs require rapid rotation of the He core and removal of the H envelope. Both criteria are satisfied by Pop III HMXBs, and it is plausible that massive Pop III stars in binary systems are dominant LGRB progenitors in the early Universe (Bromm & Loeb 2006). Our results on HMXB formation rates can therefore be used to predict and interpret observations of high-redshift LGRBs.

The paper is organized as follows. We start in §2 by discussing the problem to be solved—beginning with the

equations of motion, followed by the description of our N -body code, our choices for the initial conditions, and how the data is interpreted for HMXB formation. We present our results in §3. In §4, we discuss the implication of our work for the X-ray output of the first galaxies, as well as for other topics such as LGRBs and SMBH formation. We conclude with a summary of our findings in §5.

2 STELLAR DYNAMICS

Here, we provide an overview of our simulations—namely: the equations of motion that are solved to simulate the dynamical evolution of the star groups; the numerical scheme we use to solve the equations; the different types of initial conditions we adopted, as well as the reasoning behind our choices; and finally, how the results are interpreted for HMXB formation.

2.1 The equations of motion

Our N -body code computes the motion of N objects with (generally different) masses m_i , moving under their mutual gravitational influence, a dissipative dynamical friction force, and a background gravitational potential. We numerically integrate the equations of motion

$$\frac{d^2}{dt^2} \vec{r}_i = \vec{a}_{g,i} + \vec{a}_{df,i} + \vec{a}_{bg,i}. \quad (1)$$

The first term on the right-hand side of equation (1) is the specific force due to Newtonian gravity,

$$\vec{a}_{g,i} = - \sum_{j \neq i} G m_j \frac{\partial S(r_{ij})}{\partial r_{ij}} \frac{\vec{r}_i - \vec{r}_j}{r_{ij}}, \quad (2)$$

where G is the gravitational constant, \vec{r}_i is the displacement of the i_{th} star from the center of the host dark matter halo, and $r_{ij} \equiv |\vec{r}_i - \vec{r}_j|$.

We adopt the Plummer softening kernel $S(r_{ij})$ (e.g. Binney & Tremaine 1987),

$$S(r_{ij}) = - \frac{1}{\sqrt{r_{ij}^2 + \epsilon^2}}, \quad (3)$$

where we take $\epsilon = R_\odot$.

The second term on the right-hand side of equation (1), $\vec{a}_{df,i}$, is the specific drag force due to dynamical friction. For collisionless systems, the standard Chandrasekhar formula for dynamical friction is (Binney & Tremaine 1987),

$$\vec{a}_i = -4\pi \ln \Lambda f(X_i) \frac{G^2 m_i}{v_i^3} \rho(r_i) \vec{v}_i, \quad (4)$$

where

$$f(X_i) \equiv \text{erf}(X_i) - \frac{2}{\sqrt{\pi}} X_i \exp(-X_i^2), \quad (5)$$

v_i is the speed of the i_{th} star with respect to the background, $X_i \equiv v_i/(\sqrt{2}\sigma_v)$, σ is the velocity dispersion, $\ln \Lambda$ is the Coulomb logarithm and $\rho(\vec{r}_i)$ is the local gas density.

We adopt the modified formula for gaseous medium used in Tanaka & Haiman (2009). This prescription incorporates behaviors found in numerical simulations for subsonic and supersonic regimes (Ostriker 1999; Escala et al. 2004).

The specific drag force vector always points opposite to the direction of motion, and is given by:

$$a_{df,i}^{(gas)} = -4\pi G^2 m_i \rho(\vec{r}_i) \frac{1}{v_i^2} \times f^{(gas)}(\mathcal{M}_i), \quad (6)$$

with

$$f^{(gas)}(\mathcal{M}_i) = \begin{cases} 0.5 \ln \Lambda \left[\text{erf}\left(\frac{\mathcal{M}_i}{\sqrt{2}}\right) - \sqrt{\frac{2}{\pi}} \mathcal{M}_i \exp\left(-\frac{\mathcal{M}_i^2}{2}\right) \right] & 0 \leq \mathcal{M}_i \leq 0.8; \\ 1.5 \ln \Lambda \left[\text{erf}\left(\frac{\mathcal{M}_i}{\sqrt{2}}\right) - \sqrt{\frac{2}{\pi}} \mathcal{M}_i \exp\left(-\frac{\mathcal{M}_i^2}{2}\right) \right] & 0.8 \leq \mathcal{M}_i \leq \mathcal{M}_{eq}; \\ \frac{1}{2} \ln \left(1 - \frac{1}{\mathcal{M}_i}\right) + \ln \Lambda & \mathcal{M}_i > \mathcal{M}_{eq}. \end{cases} \quad (7)$$

Above, $\mathcal{M}_i \equiv v_i/c_s$ is the Mach number, and c_s is the sound speed. We use $\ln \Lambda = 3.1$ and the corresponding value of $\mathcal{M}_{eq} \approx 1.5$.

In our simulations, the motion of the stars with respect to the background gas is supersonic. In this regime, the characteristic dynamical friction timescale, for a circular Keplerian orbit of two bodies with for $m_1 \gg m_2$ and $v_2 \gg c_s$, is

$$\tau_{df} \sim \frac{E_{orb}}{P_{df}} \sim \frac{1}{80} \sqrt{\frac{m_1^3}{m_2^2 G}} \frac{1}{\rho(r_2) r_{12}^{3/2}}, \quad (8)$$

where P_{df} is the frictional dissipation power ($m_2 a_{df,2} v_2$), and E_{orb} the orbital energy ($Gm_1 m_2 / 2r_{12}$).

The third and last term, $\vec{a}_{bg,i}$, is the specific force due to the background potential, which is dominated by gas. The background potential provides an additional inward force whose functional form depends on the density profile. For simplicity, here we use a constant density and explore different values in our simulations. The force due to the background potential is then

$$\vec{a}_{bg,i} = -4\pi G \rho \vec{r}_i, \quad (9)$$

where here \vec{r}_i is the vector pointing from the center of the halo to the i -th star.

The equation of motion is solved iteratively, with the positions, velocities and accelerations of each star updated at every time step. We describe our computational method below.

2.2 Code Description

We perform 3-dimensional, N -body simulations with 4th-order & 5-stage Runge-Kutta-Fehlberg methods (RKF45 method, Erwin 1969) using adaptive time steps. The RKF45 is a very precise and stable integration method among the large class of Runge-Kutta schemes, particularly by adapting the Butcher tableau for Fehlberg's 4(5) method.

We solve equation (1), as described in the preceding text, updating the position and velocity components of the stars while treating the background density of the gas as a uniform and static distribution.

To ensure numerical precision, our computational scheme varies the value of each subsequent time step analytically, so that numerical errors for each variable in the

simulation do not exceed 10^{-13} times the size of the variable. In some cases, however, this method leads to excessive computational effort for calculating relatively trivial interactions. For example, near the pericenter of hyperbolic or highly elliptical encounters, the time steps become increasingly small in a runaway fashion to compensate for the steep rise in acceleration and associated errors. In order to avoid such situations, we implement the following two numerical shortcuts to keep computation times tractable.

The first shortcut is to use analytic approximations for very close 2-body encounters. This is justified in cases where pairs of stars are sufficiently close to each other and isolated from the other stars in the simulation, so that (i) the gravitational pull from the other stars and the background potential are negligible compared to the mutual gravitational pull of the pair, and (ii) the orbital motion is supersonic and the dynamical friction force can be treated as a linear perturbation to the 2-body Keplerian problem. The code employs analytic approximations for any close stellar pairs that satisfy these conditions, and reverts to the RKF algorithm when the conditions stop being satisfied.

We derived the following approximations for the semi-major axis and the eccentricity:

$$a(t) = \left[a(t_0)^{-3/2} + \beta \rho \sqrt{\frac{G}{\tilde{\mu} w(q)}} (t - t_0) \right]^{-2/3}, \quad (10)$$

$$e(t) = \sqrt{1 - \frac{a(t)}{a(t_0)} (1 - e(t_0)^2)}. \quad (11)$$

Above, $\tilde{\mu}$ is the reduced mass, $a(t_0)$ and $e(t_0)$ are respectively the semi-major axis and the eccentricity at $t = t_0$, β is a dimensionless constant, and $w(q)$ is a function of the mass ratio that is symmetric about $q = 1$. Note that the variable a with subscript indicates the specific force, while without subscript it represents the semi-major axis. To derive the analytical expression for the time-evolution of the orbital distance in equation (10), we integrated the equation of the motion of a star under the influence of a dynamical friction torque. Equation (11) then follows from the definition of orbital eccentricity in terms of orbital energy and angular momentum. Note that as the radial distance decreases, the eccentricity increases. Here, β and $w(q)$ are free parameters and we use $\beta = 0.035$ and $w(q) = q^{1.4} + (1/q)^{1.4}$. The stellar coordinates and velocities are recovered as functions of a and e using standard expressions for Keplerian orbits (Binney & Tremaine 1987).

Because we are dealing with systems with more than three bodies of different masses, stars frequently form hierarchical triple systems whose motions are affected by the Kozai mechanism (Kozai 1962). Since our analytic solutions above do not account for such changes in mutual inclination, we limit the use of these solutions to situations where $\tau_{\text{outer}} < \tau_{\text{Kozai}}$, where τ_{outer} is the dynamical timescale for the outer pair in the hierarchical triple, and τ_{Kozai} is the time scale for the Kozai mechanism,

$$\tau_{\text{Kozai}} \sim \frac{m_1}{m_2} \frac{P_{1,2}^2}{P_{1,3}} (1 - e_{1,2}^2)^{1.5}. \quad (12)$$

The subscript 1 above indicates the primary star of the inner compact binary along with the satellite star denoted by the

subscript 3, while the hierarchical tertiary star is indexed by the subscript 2, and P is the orbital period.

Our second shortcut for keeping the simulation run-times manageable is to set a minimum value for the time step. We choose a physically motivated value, $10^{-6} \times \tau_{\text{dyn, min}}$, where $\tau_{\text{dyn, min}}$ is the smallest value of the dynamical time between any two stars in the simulation (that are not being treated by the analytic shortcut above) at a given time step. This procedure is necessary when there are three or more stars interacting at small separations, in which case the analytic approximations above cannot be used. We note that such situations are rare compared to the places where the analytic shortcut is applicable.

2.3 Determining HMXB formation

It is assumed that a HMXB has formed if both of the following criteria are satisfied:

(i) *One of two stars forming a binary turns into a black hole.* In order to determine which stars turn into black holes, we need to compare the typical lifetime (τ_{life}) of a massive star with the time (t_{run}) in the simulation (taken to coincide with the time at which stars are born). If $\tau_{\text{life}} > t_{\text{run}}$, the star is marked as a black hole in the simulation. For main-sequence stars, it is possible to estimate this lifetime from the mass-luminosity relation, that is $E_{\text{star}} \sim m$ and $L_{\text{star}} \sim m^p$, leading to $\tau_{\text{life}} \sim m^{1-p}$ with $2 < p < 3$. However, due to the uncertain value of p for Pop III stars, we rather prefer to use here the nuclear time scale of Pop III stars estimated by Schaerer (2002) and Marigo, Chiosi & Kudritzki (2003). They calculate the H-burning nuclear time scale for these stars with a stellar evolution code. We assume that a BH forms if the stellar mass is greater than $8 M_{\odot}$.

(ii) *The two stars are close enough so that the accretion occurs through Roche-lobe overflow (RLOF).* This criterion is simply written as $R_{\text{star}} \geq R_{\text{RL}}$, where R_{star} is the stellar radius, and R_{RL} is the Roche-lobe radius of the most massive star calculated from the center of the star to the inner Lagrange point. An approximate analytic formula to the Roche-lobe radius of star 1 for a wide range of the mass ratio is (Eggleton 1983),

$$\frac{R_{\text{RL},1}}{r} = \frac{0.49q^{2/3}}{0.6q^{2/3} + \ln(1 + q^{1/3})}, \quad (13)$$

where r is the orbital distance and $q = \frac{m_2}{m_1}$ is the mass ratio. Although the above expression was derived in a study of binaries in circular orbits, Regös, Bailey & Mardling (2005) found that the Roche lobe radius does not differ very much for eccentric binaries. We therefore apply equation (13) to all binaries found in our simulation.

If a binary satisfies these two criteria, the binary is marked as a HMXB. Since the two criteria are independently checked at every time step, which criterion is satisfied first is not important.

2.4 Setup and Initial Conditions

We design our simulations with the $20 \lesssim z \lesssim 30$ Universe in mind. This is the redshift range where the dark matter haloes reach virial temperatures $\sim 1000 - 2000$ K, the expected condition for Pop III formation, at the highest rates.

The lifetimes of the stars are several Myr, which is comparable to the timescales on which the host haloes undergo mergers with other Pop III forming haloes (Tanaka 2014).

The initial positions of the stars are generated quasi-randomly via a Monte Carlo realization as follows, motivated by the assumption that they formed inside a shared Keplerian gas disk at the center of the host dark matter halo. Their initial radial positions in the disk plane are chosen randomly from a uniform distribution whose amplitude depends on the characteristic size scale of the star-forming cloud (see below). Their azimuthal distribution is chosen to be nearly uniformly distributed, so that the azimuthal angular position of the n -th star is given by $360^\circ(n/N) \pm 5^\circ$, where N is the total number of stars in the group. This choice is made to minimize the radial gravitational pull between the stars, so that they do not immediately fly apart. Naturally, the azimuthal positions do not remain evenly spaced, but become mixed quickly. Finally, we allow the stars to be displaced out of the plane of the disk. Their positions perpendicular to the plane are chosen randomly, so that their vertical displacement out of the disk plane is no more than 5% above or below their initial radial displacement from their shared center of mass. The initial velocities of the stars are assigned to be circular, parallel to the disk plane, and Keplerian at the instant the simulation begins.

For this study, we investigated two different size scales of star forming regions.

(i) *Large scale*: Following the results from Stacy & Bromm (2013), where Pop III protostars are formed inside star-forming regions with a size of a few thousand AU, we have performed simulations where the stars are placed inside a region of size ~ 2000 AU.

We explore two different values of uniform, constant gas density, 10^6 cm^{-3} (denoted n_6 hereafter) and 10^4 cm^{-3} (n_4).

For gas of primordial composition, the molecular weight μ can vary between 0.6 and 1.2, depending on the ionization fraction. We adopt $\mu = 1$ for simplicity; this choice does not qualitatively affect our results, since our values for n are selected arbitrarily with the goal of exploring the qualitative dependence on n .

Each simulation is run for 5 Myr. The masses of the stars follow the initial mass function (IMF) they provide with $\alpha = 0.17$ ($\frac{dN}{dM} = M^{-\alpha}$), $M_{\text{max}} = 140 M_\odot$ and $M_{\text{min}} = 0.1 M_\odot$. For these simulations, we consider $N = 5$ stars.

(ii) *Small scale*: In the simulations by Greif et al. (2012), multiple protostars formed several AU apart from each other. We therefore run a second set of simulations, where stars form within a 10 AU radius. Since Greif et al. (2012) do not provide a slope for the IMF, we use $\alpha = 0.17$ as above. That study found that more than half of the mass accreted during the protostar phase goes to the most massive protostar in the group.

To mimic this behavior, we first generate a star with $M_{\text{max}} = 200 M_\odot$, then generate each subsequent star with $M_{\text{max}} = 200 M_\odot -$ [the sum of the masses of the previously generated stars].

Just as with the large-scale case, we run simulations with number densities n_6 and n_4 . Because this case is the more relevant one for forming HMXBs, we explore several different configurations: cases with a star group of $N = 5$ stars, a star group of $N = 10$ stars, and collisions between two groups

Large scale	n_6	n_4
number of runs	20	23
$P(\text{B}_{12}) [P(\text{B}_{12} + \text{B}_{13})]$	0.60(0.90)	0.56(0.74)
$\langle a_{t=5\text{Myr}} \rangle [\text{AU}]$	270	340

Table 1. Summary of the large scale calculations for $n = 10^6 \text{ cm}^{-3}$ (n_6) and $n = 10^4 \text{ cm}^{-3}$ (n_4). $P(\text{B}_{12})$ denotes the fraction of the simulations in which the most compact binary consists of the two most massive stars. We also list $P(\text{B}_{12} + \text{B}_{13})$, the fraction where the most compact binary consists of the most massive star paired with either the second or third most massive star. Also shown is the average semi-major axis of the most compact binary at $t = 5$ Myr.

of $N = 5$ stars. The last case is motivated by the fact that Pop III-forming minihaloes undergo frequent mergers, which suggests that the nascent star groups themselves undergo close encounters.

3 RESULTS

Here, we summarize the findings of our N -body simulations, focusing in particular on the properties of the most compact binaries found for each set of runs.

3.1 Large scale

We ran 20 simulations for n_6 and 23 for n_4 .

For n_6 , in 12 out of 20 runs, the two most massive stars (S_1 and S_2 , where S_i is the i -th most massive star) form the most compact binary—we denote such a binary with the notation B_{12} . Similarly, binaries of type B_{13} (i.e. made up of the most massive star S_1 and the third most massive star S_3) form the most compact binary in 6 of the runs.

The left panel of Figure 1 shows a sample set of stellar trajectories for one of the large scale n_6 runs. Throughout the simulation, the compact binary tends to remain near the center of the halo, as less massive stars repeatedly undergo 3-body interactions with the binary. The fact that they do not stray far from the center of the halo is a combined effect of the background potential and the gravitational potential of the massive binary. It is these 3-body encounters that cause the most compact binary in the simulations to end up as type B_{12} or B_{13} . In two of the runs, the most compact binaries after 5 Myr consist of less massive stars.

The average value of the semimajor axis after $t = 5$ Myr in the large scale, n_6 runs is $\langle a_{t=5 \text{ Myr}} \rangle = 270$ AU, and the minimum value of a across the 20 runs is 60 AU. These values for a are much larger than that necessary for RLOF to take place, ~ 0.07 AU. Their characteristic dynamical friction time scales are roughly 10^{13} yrs, which is much longer than their lifetimes (see equation 13 when $R_{\text{RL}} = R_{\text{star}}$ and equation 8). We therefore conclude that in systems of $N = 5$ stars and $n \sim 10^6 \text{ cm}^{-3}$, with the stars initially separated at hundreds of AU, HMXBs are unlikely to form.

For the n_4 case, the fraction of runs where the most compact binary after 5 Myr is type B_{12} or B_{13} are similar to the n_6 simulations: 13/23 for B_{12} , and 17/23 for B_{12} or B_{13} .

However, the dynamical evolution is quite different, as

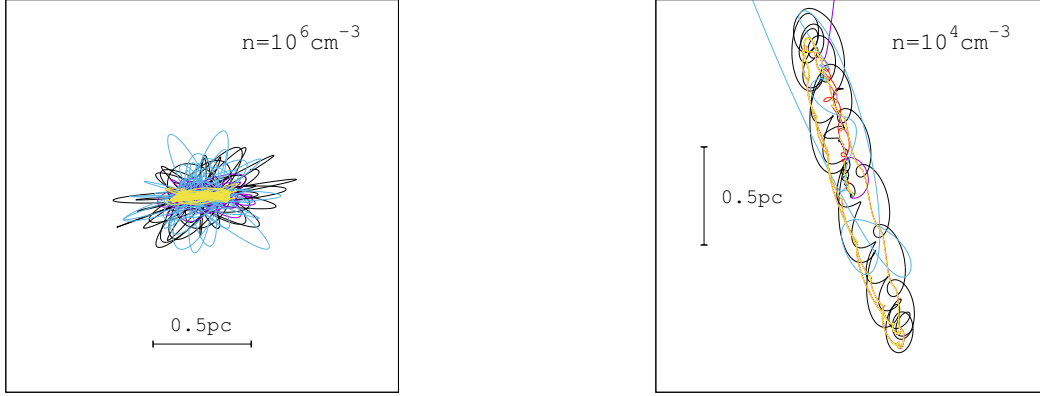


Figure 1. *Left:* Sample trajectories for large scale calculations with the high number density $n = 10^6 \text{ cm}^{-3}$ (case n_6). As shown in the figure, stars tend to stay near the center of the halo and their overall motions are oblate-spheroidal in shape. *Right:* Sample trajectories for the low number density $n = 10^4 \text{ cm}^{-3}$ (n_4). Even though stars including binary systems remain within a certain distance range, they are not as close as the stars in the higher density calculation, leading to less frequent three-body interactions. Furthermore, one can notice that a few stars (blue line and purple line) are kicked off.

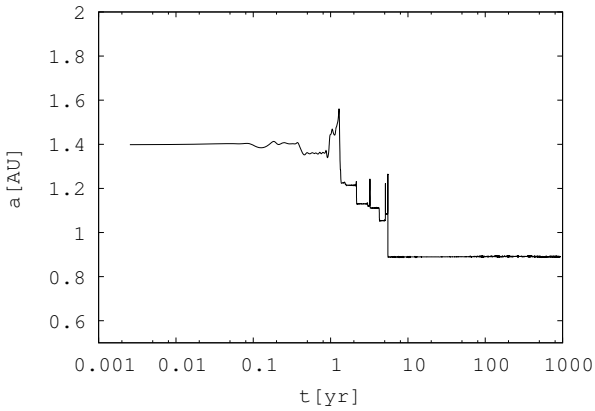


Figure 2. Evolution of the semi-major axis of a typical binary in a system. The sharp variations are due to stellar scatterings, which mostly result in a hardening of the binary. After the multiple system gets stabilized and isolated (which happens after ≈ 10 years), the decrease rate of the semi-major axis depends on dynamical friction alone.

can be seen by the right panel of Figure 1. The lower gas densities lead to weaker forces due to dynamical friction and background potential, and stars (especially less massive ones) tend to be scattered farther from their initial position, as far as $\gtrsim 1 \text{ pc}$. This also results in less frequent three-body interactions in general, and may explain the larger average value of the semi-major axis after 5 Myr, $\langle a_{t=5\text{Myr}} \rangle = 340 \text{ AU}$. The formation of HMXBs appears even more intractable for the n_4 case.

Sample stellar trajectories for the n_6 and n_4 large scale cases are shown in Figure 1, and a summary of the results is given in Table 1.

3.2 Small scale

For the small scale case, we performed 86 runs of 5-body simulations for each of the number density values n_6 and

Small scale	n_6	n_4
runs	86	86
$\langle a_{t=500\text{yr}} \rangle [\text{AU}]$	1.37	1.42
$\tau_{\text{df}} [\text{yr}]$	$\sim 10^{13}$	$\sim 10^{15}$
Companion stars	3rd massive star, 11 $\sim 12 M_{\odot}$	
P_{HMXBc}	0.070	0.070
$F_{\text{HMXB}} [10^{-4} M_{\odot}^{-1}]$	4.6	4.6

Table 2. Summary of results for simulations of 5-body groups forming on small scales. $\langle a_{t=5000 \text{ yr}} \rangle$ indicates the semi-major axis at $t = 5000 \text{ yr}$, while τ_{df} represents the dynamical friction timescale required for $a_{t=5000 \text{ yr}}$ to shrink to a_{RL} (see equation 8). P_{HMXBc} is the fraction of runs in which a HMXBc forms, and F_{HMXB} is the number of HMXBc formed across all simulations, normalized by the total mass of the stars in the simulations.

n_4 . Due to the smaller initial separations of the stars, we run the simulations for a shorter amount of time.

We run each simulation for a minimum of 1000 yr, but stop the run if a stable binary forms, and if no further significant dynamical changes are observed. If such a binary does not form, we run the simulations to a maximum duration of 5000 yr.

In order to properly compare the results from the n_6 calculations with those from the n_4 calculations, we use the same initial conditions for each set of runs.

In the n_6 calculations, the most common scenario is that S_1 always forms the most compact binary almost immediately, while stellar scatterings are most common during the first few years to about 40 years. Thereafter, a multiple system usually survives and stabilizes, while less massive stars are ejected. A difference between the large-scale and the small-scale scenarios is that, whereas most cases in the large-scale calculations end up with one binary and unbound single stars (in 15 out of 20 cases), in the small-scale runs a multiple system such as triple or quartet (rather than a simple binary) forms (in 59 of 86 cases). Less massive stars take

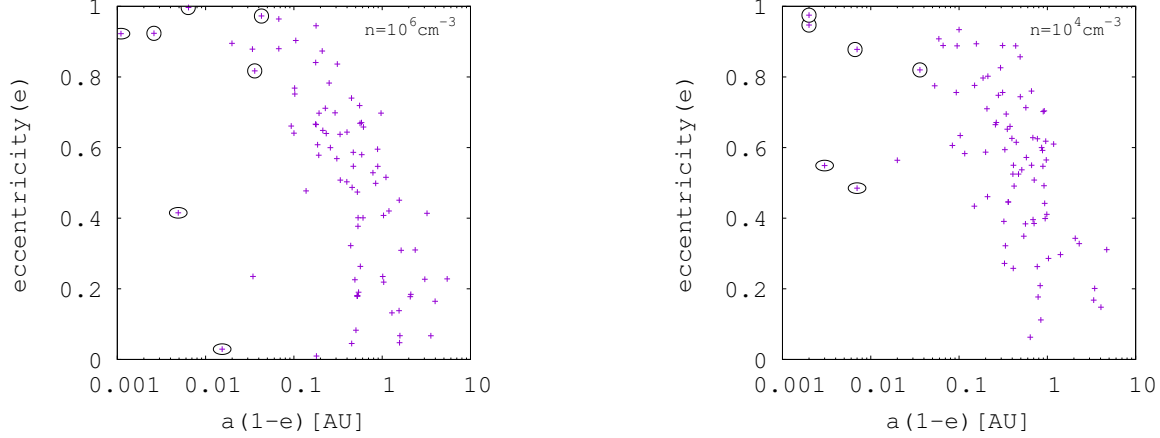


Figure 3. *Left:* Pericenter distance - eccentricity distribution plot for n_6 . Two HMXB candidates (HMXBc) have been produced. *Right:* The same distribution plot for n_4 . The circled points indicate HMXBc whose mass transfer via RLOF may occur periodically due to their eccentric orbits. The elliptically-circled point indicates an HMXBc whose semimajor axis is smaller than a_{RL} , so the mass transfer will be steady. There are a couple of binaries with pericenter distance smaller than R_{RL} , but they are excluded because $M_2 < 8 M_{\odot}$.

some energy from the multiple system and convert it into their kinetic energies while causing the binary to harden.

As an example, Figure 2 shows the evolution in the semi-major axis of a compact binary in one of the runs. One can easily notice the quick decrease in the semi-major axis during violent stellar interactions (before 10 years), which clearly indicates the hardening. After a couple of stars are cast away and the multiple system is stabilized and isolated (after about 10 years), dynamical friction plays the main role in the decrease of the semi-major axis; after this point, we do not expect further dramatic hardening of the binary. In our 86 runs, the last surviving binary is typically of type B₁₃ (pairing of the most massive and third most massive stars), with total mass of $130 M_{\odot}$ and $\langle M_{\text{S}_3} \rangle = 11 M_{\odot}$. $\langle a_{t=5000 \text{ yr}} \rangle = 1.87 \text{ AU}$ and the minimum semi-major axis is 0.2 AU . The corresponding dynamical friction time scale (equation 8) is $\sim 10^{13} \text{ yr}$. The ejected stars have speeds of $(10-100) c_s$, and $c_s \sim 4 \text{ km/s}$. Six of the HMXB candidates (HMXBc hereafter) have been formed in all runs ($P_{\text{HMXBc}} = 0.070$). For later use, let us define F_{HMXB} as the number of HMXBc formed across all simulations, normalized by the total mass of the stars. Then $F_{\text{HMXBc}} = 4.6 \times 10^{-4} M_{\odot}^{-1}$ (This term will be used to estimate the X-ray luminosity and is one of the primary results of our study).

The outcomes of the n_4 simulations are quite similar: a triple or higher multiple forms in 65 of 86 runs, and $\langle a_{t=5000 \text{ yr}} \rangle = 1.42 \text{ AU}$. Furthermore, due to the same number of HMXBc, P_{HMXBc} and F_{HMXBc} are the same. One notable difference is that for n_4 , the dynamical friction time scale is longer by 2 orders of magnitude compared to n_6 , because this quantity is inversely proportional to the number density.

Interestingly, there are four runs (for each density value) in which the most compact binary is eccentric, and inside the requisite separation for RLOF at pericenter but outside it at apocenter. We consider only two of them as HMXBc and rule out the other two binaries since the mass of the more massive star is smaller than $8 M_{\odot}$ (Heger et al. 2003). We present the distribution of eccentricity for pericenter distance in Figure 3. In particular, the *left* panel shows the dis-

tribution for n_6 calculations and the *right* panel for n_4 . The circled point indicates HMXBc with distance at pericenter shorter than the corresponding Roche-Lobe radius.

How accretion proceeds in a highly eccentric binary system under these conditions remains an unsettled issue to date, as studies have claimed that the orbital semimajor axis and eccentricity can either increase or decrease depending on the binary properties at pericenter (Sepinsky, Willems & Kalogera 2007 and Sepinsky et al. 2009). If the RLOF does induce circularization, then accretion proceeds normally (i.e. steadily). However, if the RLOF instead increases the eccentricity of the system, then, whether accretion can proceed steadily rather than intermittently will depend on the relative timescale between the disk lifetime τ_{disk} (on the order of the viscous timescale), and the orbital period of the binary t_{orb} . We computed these timescales for all the eccentric binaries in our simulations (for which the Roche-Lobe radius straddles the pericenter and apocenter), and found that $\tau_{\text{disk}} > t_{\text{orb}}$ in all cases but one.

This implies that the fraction of binaries whose eccentricities cause intermittent RLOF is small, and that as a global average, RLOF is steady to a good approximation.

The magnitude of the gas density considerably influences the characteristics of the dynamical interactions. While on the one hand 40% of the simulations end up forming the same triples for both density values, on the other hand their trajectories and the center of mass movements differ significantly. Figure 4 shows two sample trajectories of 5 stars with low number density (left panel) and high number density (right panel) after 1000 yr. They were given identical initial conditions for the run, but their trajectories have developed differently. In Figure 5, at 800 yr, even though the same stars form a triple and the same star is ejected for both number densities, their trajectories are clearly different.

As can be seen in Figure 6, which shows the change of forces per unit mass exerted on a typical kicked-off star, a_{df} and a_{bg} are negligible compared to a_{gr} before about 5 years.

Note that a_{df} and a_{bg} are synchronized at early times because the motions of the stars are close to the Keplerian motion, $r \sim 1/v^2$. The star in Figure 6 is ejected at $t \approx 10 \text{ yr}$

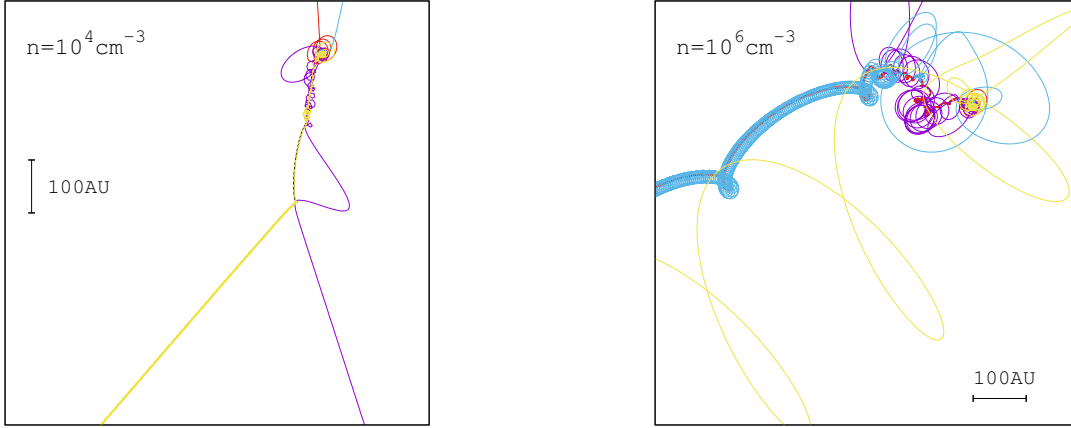


Figure 4. Trajectories up to $t = 2000$ yr for 5-body simulations with identical initial conditions but different densities: n_4 (left panel) and n_6 (right panel). Despite having the same starting point, the trajectories of the 5 stars evolve quite distinctly in the two backgrounds due to the different magnitudes of dynamical friction. The two simulations for different bound systems: a binary for n_4 (yellow line) and a quartet for n_6 (red+blue+yellow lines).

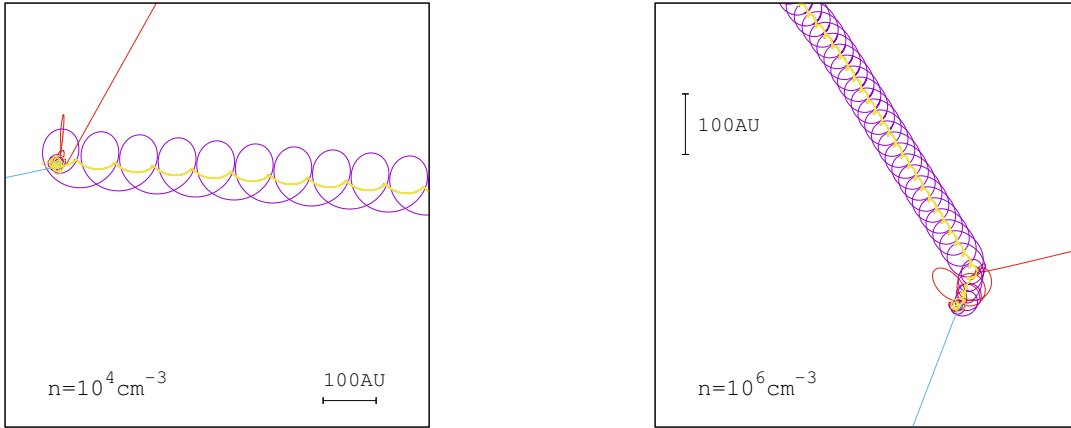


Figure 5. Trajectories of two 5-body simulations with identical initial conditions but different ambient gas densities. The simulations have formed triples with the identical stars (yellow+purple lines; contrast with 4) at $t = 1000$ yr, despite differences in the trajectories of each star and the center of mass.

for the high number density (and at $60 \lesssim t \lesssim 80$ yr for the low number density). This can be understood from the fact that a_{gr} monotonically decreases and a_{bg} increases ($a_{\text{bg}} \sim r$ where r is the distance from the center of mass). At the same time, a_{df} barely changes since the star moves in the supersonic regime and the speed decreases slowly.

There is no noticeable difference in the overall results between the n_4 and n_6 runs—quantities such as $\langle a_{t=5000 \text{ yr}} \rangle$, the dynamical friction time scale τ_{df} , the total mass of the most compact binary (or which star forms the compact binary with S_1) as summarized in Table 2. For both number densities, the companion star of the binary is typically the third most massive star S_3 .

To sum up, we find that $P_{\text{HMXBc}} \sim 7\%$ of our simulations form HMXBc, regardless of the gas density value. Normalized to the total stellar mass in the simulations, the number of HMXBc formed per stellar mass is $F_{\text{HMXB}} \approx 4.6 \times 10^{-4} M_{\odot}^{-1}$.

3.3 10-body simulations

We now explore several different configurations for the star group, and run several sets of simulations with 10 stars (instead of 5). These are: (1) 10-body version of the small scale calculation presented above; (2) head-on crash of two star groups containing 5 stars each; (3) a close encounter and subsequent inspiral and merger of two star groups containing 5 stars each. The latter two scenarios are motivated by the fact that the merger timescales and mass accretion timescales of Pop III host haloes, as well as the lifetimes of the massive Pop III stars themselves, are of the same order, ~ 10 Myr. This suggests that merging haloes will be continuously forming new stars (perhaps Pop II instead of Pop III) as they merge with other haloes, and that close interactions and mergers of nascent star groups may be relatively common. We generate stellar masses in the same way as for the 5-body case, but with a larger value for the parameter $M_{\text{max}} = 300 M_{\odot}$. We have run each simulation for

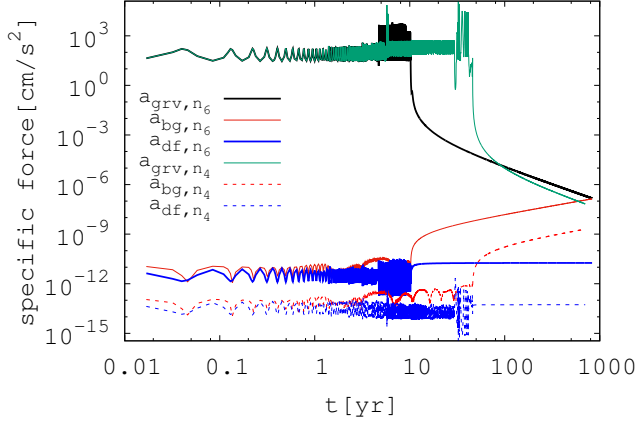


Figure 6. Changes with time in the three forces per unit mass (gravity from other stars, dynamical friction and background gravity) acting on star₄ (the light blue color line in Figure 5). We run two simulations with identical initial conditions but different ambient gas densities n_4 and n_6 . During the early phases of the interaction, the gravitational force (a_{gr}) dominates by several orders of magnitude over dynamical friction (a_{df}) and the background force (a_{bg}). Note that a_{gr, n_6} (black line) and a_{gr, n_4} (green line) synchronize at early times because the motion of the star is very close to Keplerian and $r \sim 1/v^2$. After the star is ejected at 10 yr for n_6 (later for n_4), a_{gr} monotonically decreases and a_{bg} increases ($a_{bg} \sim r$ where r is the distance from the center of the halo). During the same time, a_{df} barely changes since the star moves in the supersonic regime and the speed decreases very slowly.

Scenario	1	2	3	4A	4B
runs	54	30	30	30	30
$\langle a_{t=500 \text{ yr}} \rangle$ [AU]	1.0	1.1	0.90	1.8	1.6
$\langle a_{B_{12}} \rangle$ [AU]	1.6	1.5	1.8	2.4	2.0
$\langle a_{rest} \rangle$ [AU]	0.72	0.15	0.42	1.2	0.23
P_{HMXBc}	0.33	0.33	0.27	0.13	0.27
F_{HMXBc} [$10^{-4} M_{\odot}^{-1}$]	15	11	9.0	4.2	8.4

Table 3. Summary of the results from 10-body simulations. We have considered five different scenarios. Scenario 1 simulated the 10-body version of the 5-body calculation, i.e. an isolated star group. The other scenarios all involve collisions of two 5-body star groups. Scenario 2 is a head-on collision of two coplanar, co-rotating star groups. Scenario 3 also collided two groups of stars with co-rotating orbital planes, but with an impact parameter comparable to the sizes of the groups, which results in an inspiral and eventual merger. Scenarios 4A and 4B are similar to scenario 3, except that the orbital planes of the colliding star groups had mutual inclinations of 45° and 135° , respectively.

500 yr. The results of these simulations are summarized in Table 3. We briefly discuss each one, as follows.

3.3.1 Scenario 1: 10-body group in isolation

We set up the simulations as in the 5-body calculations, but with 10 stars.

We find that $\langle a_{t=500 \text{ yr}} \rangle = 1.0$ AU. Interestingly, there are 18 out of 54 cases in which $a < a_{RL}$. There is a large difference in scale between $a_{B_{12}}$ and a_{rest} , where $a_{B_{12}}$ is the

semi-major axis of B_{12} (binary made up of the two most massive stars) and a_{rest} is the semi-major axis of the binary stars other than S_1 and S_2 . This is a common feature of the 10-body simulations: they often end up with triples whose inner binary is B_{rest} while the outer binary is B_{12} . Our simulations yield $\langle a_{rest} \rangle = 0.72$ AU and $\langle a_{B_{12}} \rangle = 1.6$ AU. Also note that, in 14 out of 18 HMXBc, the binary is B_{rest} (i.e. it is not made up of the two most massive stars).

Since the compact binaries in these simulations form quickly and we only follow them for 500 years, it is technically possible that they will be disrupted before one of the stars turns into a BH. However, our simulations for the 5-body scenario showed that compact, quasi-steady binaries are unlikely to be disrupted, and for practical purposes we extrapolate this qualitative result to the 10-body case.

We find that a HMXBc forms in a larger fraction of these simulations than in the 5-body case, $P_{HMXBc} = 0.33$, for the obvious reason that there are more stars. Per unit stellar mass in the simulations, the number of HMXB candidates is $F_{HMXB} = 1.5 \times 10^{-3} M_{\odot}^{-1}$, which is a factor ≈ 3 higher than we found for the 5-body case.

3.3.2 Scenario 2: Collision between two 5-star groups – head-on collision

Two groups of 5 stars are set up with random initial conditions, in the same manner as for the previous simulations of 5-body groups. The two groups are then arranged to collide head-on, as follows: they are placed at a separation of two to three times their sizes and their disks are aligned so that the mutual inclination is zero. The initial relative speed of the groups is roughly the speed of sound and the center of mass of one group is set to move directly toward the center of mass of the other group.

We find that prior to colliding, each group forms a compact binary of type B_{12} (the most and second-most massive star). When the two groups collide, those two binaries that existed before the collision were broken and the two most massive stars of each group form a new compact binary with high chances.

The average $\langle a_{t=500 \text{ yr}} \rangle$ is 1.1 AU, but $\langle a_{B_{12}} \rangle = 1.5$ AU and $\langle a_{rest} \rangle = 0.15$ AU, meaning that the most compact binaries are not formed from the most massive stars. The shorter average separations may be a result of a larger number of early 3-body scatterings, which act to harden the group as a whole.

HMXBc form in 10 out of 30 runs, and they are not of type B_{12} . However, we find a rate of HMXB formation per stellar mass $F_{HMXB} = 1.1 \times 10^{-3} M_{\odot}^{-1}$; this is higher than in the 5-body case and comparable to Scenario 1 above. Sample trajectories for one of the simulations of scenario 2 are depicted in Figure 7.

3.3.3 Scenario 3: Collision between two 5-star groups – spirally merging case

We have used the same input parameters for the two groups as in Scenario 2, except that we now set the impact parameter to be of order the size of the group, whereas it was set to zero in Scenario 2.

The groups are given opposite velocities of $\sim c_s$ along

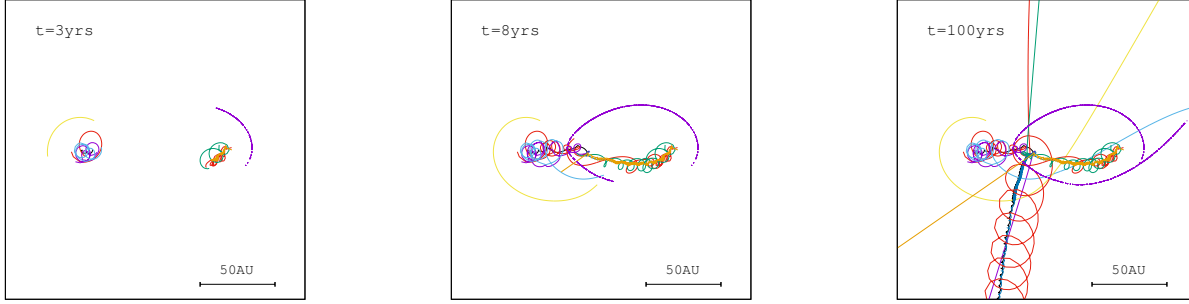


Figure 7. 10-body head-collision (scenario 2). In these sample trajectories, five stars in each group are in nearly Keplerian motion. The groups move towards each other with a relative velocity of $\sim c_s$ (left panel). At $t \approx 8$ yr (middle panel), the two haloes begin to merge. During the merger, all ten stars undergo stellar scatterings (right panel). One triple (black+dark blue+red lines) has been formed and it is moving in -y direction. In these head-on collisions, it is likely for multiple systems that existed before merging to be broken, while a few new multiple systems are formed.

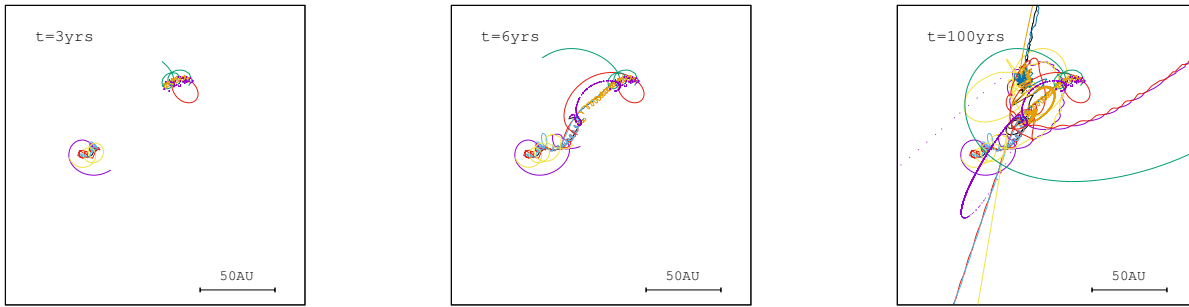


Figure 8. 10-body spirally merging case (scenario 3). As with scenario 2, two groups of 5 stars are set on a collision course. However, in this scenario the impact parameter is $\sim 2 - 3$ times the size of groups, whereas in scenario 2 it is set to be zero. The groups are approaching each other at the relative velocity of c_s (left panel). At $t = 8$ yr, the groups are about to merge (middle panel). After some time (right panel), two binaries are ejected (red and purple lines in the x -direction and black and blue lines in the y -direction). In this sample case, the most compact binary is the one ejected in the y direction (black+blue lines) with $a = 0.8$ AU at $t = 100$ yr. A difference between this scenario and the head-on collision is that compact systems are more likely to survive the merger.

the x -direction, and are offset by a displacement along the y -direction that is $\sim 2 - 3$ times the typical size of the star group (~ 20 AU) so that they merge with a spiral motion.

We find that $\langle a_{t=500 \text{ yr}} \rangle = 0.90$ AU, $\langle a_{B_{12}} \rangle = 1.8$ AU and $\langle a_{\text{rest}} \rangle = 0.42$ AU.

The average separation lies between what we find in Scenarios 1 and 2. This can be interpreted as being due to the fact that these simulations (in which the two groups merge gradually via inspiral) have more close 3-body interactions than in Scenario 1 (in which 10 stars in quasi-Keplerian orbits evolve in isolation) but fewer such interactions than in Scenario 2 (in which the two groups merge head-on).

HMXBs form in 8 out of 30 runs and, as with Scenarios 1 and 2, none of the HMXBs are made up of the two most massive stars. We find a similar HMXB formation rate per stellar mass, $F_{\text{HMXB}} = 9.0 \times 10^{-4} M_{\odot}^{-1}$. Sample trajectories from one of the simulations for Scenario 3 are shown in Figure 8.

3.3.4 Scenarios 4A and 4B: Collision between two 5-body groups – spirally merging case with inclinations of 45 degrees and 135 degrees

In these two scenarios, we again set two groups of five stars each on a collision course. The difference is that the orbital plane of one star group is tilted, so that the two stellar disks

have a mutual inclination i . We set the inclination at $i = 45^\circ$ (nearly co-rotating) for scenario 4A, and $i = 135^\circ$ (nearly counter-rotating) for scenario 4B. The groups are initially placed at a separation of two to three times their sizes, and set in motion at the same speeds as for the inspiral case (scenario 3).

We find that $\langle a_{t=500 \text{ yr}} \rangle = 1.8$ AU, $\langle a_{B_{12}} \rangle = 2.4$ AU, and $\langle a_{\text{rest}} \rangle = 1.2$ AU for scenario 4A. In scenario 4B, we find $\langle a_{t=500 \text{ yr}} \rangle = 1.6$ AU, $\langle a_{B_{12}} \rangle = 2.0$ AU, and $\langle a_{\text{rest}} \rangle = 0.23$ AU. In 70% of the runs for both scenarios, the two most massive stars form the most compact binary. Stellar binaries end up with somewhat closer separations in the nearly counter-rotating case, due to the fact that the net angular momentum of the merged star group is smaller. Indeed, we find a total of four HMXBc across all the $i = 45^\circ$ simulations, and eight in a same number of $i = 135^\circ$ simulations.

For the same reason, we find a larger fraction of HMXB candidates per stellar mass simulated in the nearly counter-rotating case ($F_{\text{HMXB}} = 8.4 \times 10^{-4} M_{\odot}$) compared to the nearly co-rotating case ($F_{\text{HMXB}} = 4.2 \times 10^{-4} M_{\odot}$). The overall formation rate of HMXB candidates is lower for both cases than the cases in which all the stellar orbits were nearly coplanar (Scenarios 1, 2 and 3), plausibly due to the additional degree of freedom in the stellar orbits. Still, the value of F_{HMXB} is within a factor of a few for all of our simulations.

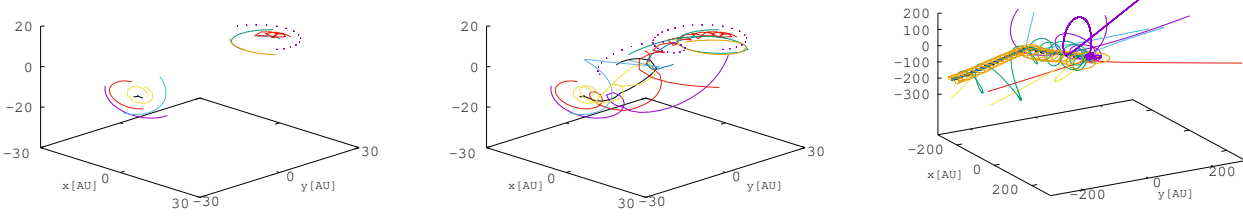


Figure 9. Trajectories for scenario 4A, a collision between two 5-body groups, each on quasi-Keplerian orbits, but with the orbital plane of the two groups tilted with respect to each other at an inclination $i = 45^\circ$. The setup is the same as scenario 3, except for the mutual inclination of the orbital planes of the colliding star groups. The left panel shows the two groups on a collision course. At $t = 4$ yr, the halos are about to merge (middle panel). After $t = 10$ yr (right panel), a triple having the most compact binary are ejected [black and blue lines (inner binary) and brown line].

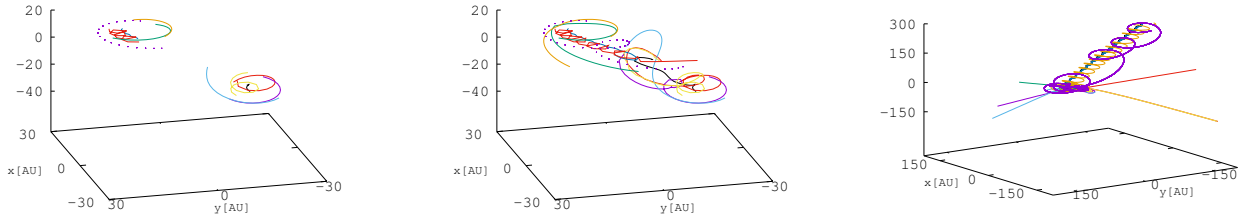


Figure 10. Trajectories for scenario 4B—the same as scenario 4A (Figure 9), but with the two groups nearly counter-rotating with respect to each other ($i = 135^\circ$). At $t = 4$ yr, the groups are about to merge (middle panel) and after $t = 10$ yr (right panel), a quartet containing the most compact binary is ejected toward the upper right of the panel [black+blue lines (inner binary), brown and thick purple lines].

Sample trajectories from runs for scenarios 4A and 4B are depicted in Figure 9 and Figure 10, respectively.

4 DISCUSSION

4.1 Binary evolution and formation of HMXB candidates

Our large-scale simulations show that the if Pop III stars form hundreds of AU apart, as in the simulations of Stacy & Bromm (2013), then the timescales required to make HMXBs via stellar scatterings are simply too long. On the other hand, if protostellar clouds fragment and form stars in close groups on scales of $\gtrsim 10$ AU, as in Greif et al. (2011), then a small fraction of groups can form HMXBs. We briefly discuss the dynamics of HMXB formation in our simulations, then move on to discuss the astrophysical implications of our findings.

The simulations indicate that, as expected, scatterings play a major role in making a compact binary. The background potential and the dynamical friction play a secondary role, by allowing the most compact binary (or triple) to remain near the center of mass of the halo and for other stars to return and scatter again and again.

We find that on average, the number of HMXB candidates formed per stellar mass, F_{HMXB} , is a function of the number and orientation of close 3-body encounters. Our re-

sults indicate that F_{HMXB} may be somewhat higher in configurations that result in fewer ejections of stars, and if the interactions are coplanar. While we are able to interpret this, as well as trends in the average separation between stellar pairs, in terms of the initial kinematic setup of the various scenarios simulated (see §3.3 above), the value of F_{HMXB} does not vary by more than a factor ≈ 3 . We interpret this lack of a significant variation in F_{HMXB} , for such a diverse set of initial conditions and ambient gas densities, to mean that our values are not far from the one that results from similar stellar encounters in nature.

4.2 The effect of migration on the formation of HMXBs

Another way in which a nascent stellar group could harden is migration through a gaseous disk. The migration could occur as the protostars form—Greif et al. (2012) found significant accretion from the protostellar disk onto the most massive protostar, and did not follow the evolution of the system beyond this stage. (It could also occur to a lesser degree in a vestigial gas disk, after the stars are in place.)

We evaluate the possible role of disk migration on the separation of Pop III stars by considering a steady, geometrically thin disk with an α viscosity (Shakura & Sunyaev 1973; see also Frank, King & Raine 2002). We adopt a disk with $\alpha = 0.01$ and an accretion rate $\dot{m} \sim 10^{-3} M_\odot \text{ yr}^{-1}$, follow-

ing Tan & McKee (2004) and Tan & Blackman (2004), who considered the structure of accretion disks around Pop III stars at high redshifts.

We estimate the migration timescale τ_{mig} following Syer & Clarke (1995). We take a binary system with primary mass $M_1 = 120 M_\odot$ and secondary mass $M_2 = 11 M_\odot$, based on the mean values found across our simulations. For these masses and disk parameters, the secondary is able to clear a gap around its orbital path (e.g. Syer & Clarke 1995; Seager 2010; Lubow & Ida 2010), by satisfying both of the following two conditions:

$$(1) \quad \frac{H}{R} \leq \left(\frac{q}{\alpha}\right)^{1/2}, \quad (14)$$

$$(2) \quad \frac{H}{R} \leq \left(\frac{q^2}{\alpha}\right)^{1/5}. \quad (15)$$

where R is the distance of the secondary from the primary, H is the scale height of the disk at that location, and $q = M_2/M_1 \sim 0.1$ is the binary's mass ratio. If condition (1) is violated, the gap will be closed by the radial pressure gradient. Condition (2) relates the gap width and the Roche radius of the secondary; this ensures that the secondary acts to transfer orbital angular momentum through the disk, rather than accreting mass via RLOF. We find that inside $R \sim 15$ AU, for the disk properties stated above, H/R is smaller than the right-hand side of equation (14) by a factor $\gtrsim 80$, and smaller than the right-hand side of equation (15) by a factor $\gtrsim 8$, indicating that the secondary is easily able to open a gap.

The migration timescale of the secondary depends on the dimensionless parameter (Syer & Clarke 1995)

$$B \equiv \frac{4\pi\Sigma_0 R^2}{M_2}, \quad (16)$$

where Σ_0 is the local surface density of a steady-state disk around the primary, in the absence of perturbations by the secondary. For $B > 1$, the gas in the disk is able to dynamically dominate over the gravitational influence of the secondary, and the secondary is pushed inward on the viscous diffusion timescale of the disk,

$$\tau_{\text{mig},0} \sim \alpha^{-1} \left(\frac{H}{R}\right)^{-2} \Omega^{-1}. \quad (17)$$

For $B < 1$, Syer & Clarke (1995) found that the migration timescale is longer,

$$\tau_{\text{mig},1} \sim \frac{1}{B^{7/17}} \tau_{\text{mig},0}. \quad (18)$$

In Figure 11, we plot the local disk mass near the secondary, $4\pi\Sigma_0 R^2$, alongside the typical secondary mass, $11 M_\odot$ (the numerator and denominator, respectively, for the ratio B). For $R \lesssim 15$ AU, $B < 1$ and the migration timescale is expected to slow. We plot the two migration timescales $\tau_{\text{mig},0}$ and $\tau_{\text{mig},1}$ in Figure 12.

Both of these timescales are shorter than both the typical lifetimes of protostellar disks, as well as of the stars themselves. This suggests that disk migration could, in principle, lead to initial stellar separations smaller than what we have assumed, making the formation of HMXBs via stellar scatterings more favorable. On the other hand, radiative feedback from the stars could blow away the disk before significant migration can occur. We submit that the HMXB

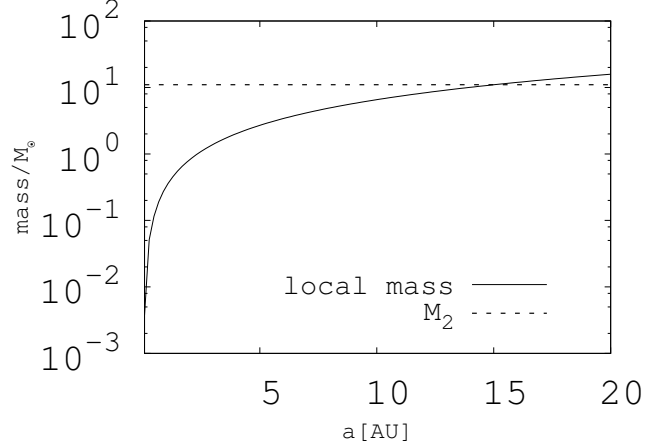


Figure 11. A comparison between the mass of a typical secondary of a binary in our simulations ($M_2 = 11 M_\odot$, dashed line) and the local mass $4\pi\Sigma_0 R^2$ (solid line) in a protoplanetary disk near its orbit. The migration timescale increases if the ratio $B = 4\pi\Sigma_0 R^2/M_2 < 1$, which is the case for close orbits.

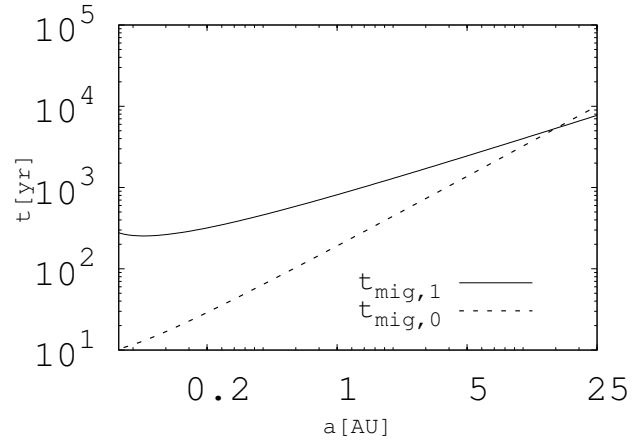


Figure 12. The migration timescales for a circumbinary protostellar disk, based on the typical binary properties of our simulations. The unperturbed Type II migration timescale, $\tau_{\text{mig},0}$ (dashed line) shows the timescale assuming that the secondary mass is much smaller than the local disk mass. A longer timescale $\tau_{\text{mig},1}$ (solid line) is expected if the secondary mass is large compared to the disk mass (see previous Figure).

formation rates inferred from our simulations be taken as a conservative estimate, with possible additional contributions from channels other than stellar scattering.

4.3 X-ray output

As discussed in §1, HMXBs are believed to be a major source of X-rays in the early universe. Observations of nearby star-forming galaxies suggest that their X-ray luminosities (which are dominated by HMXBs) scale linearly with their star formation rate (Grimm, Gilfanov & Sunyaev 2003; Gilfanov, Grimm & Sunyaev 2004; Persic et al. 2004; Mirabel et al. 2011). Mineo, Gilfanov & Sunyaev (2012) find many

studies support a linear proportionality between the X-ray luminosity of HMXBs and the star formation rate (SFR) (Grimm, Gilfanov & Sunyaev 2003, Gilfanov, Grimm & Sunyaev 2004, Persic et al. 2004 and Mirabel et al. 2011). In the linear regime, the X-ray luminosity of the local universe is given by Mineo, Gilfanov & Sunyaev (2012),

$$L_{2-10 \text{ keV}}^{\text{local}} = 3 \times 10^{39} \times \frac{\text{SFR}}{\text{M}_{\odot} \text{ yr}^{-1}}, \quad (19)$$

where SFR is the star formation rate.

How the ratio of X-ray luminosity to SFR evolves with redshift is a key question in evaluating the properties of galaxies and young stellar populations, and in linking the earliest galaxies (most of which should be actively forming stars, based on their mass accretion rates) with their X-ray luminosities. The question is as yet unresolved by current observations (Dijkstra et al. 2012; Basu-Zych et al. 2013), and is often treated as a free parameter in studies estimating the X-ray production of the first galaxies (e.g. Furlanetto 2006; Fialkov, Barkana & Visbal 2014; Tanaka, O’Leary & Perna 2015).

In the following, based on the results of our simulations, we are going to quantitatively evaluate the relation between X-ray luminosity and SFR, and compare it with equation (19). We can write the X-ray luminosity as

$$L_{2-10 \text{ keV}} = L_{\text{Edd}} \times f_{\text{Edd}} \times f_{2-10 \text{ keV}} \times t_{\text{acc}} \times f_{\text{sur}} \times f_{\text{esc}} \times F_{\text{HMXB}} \times \text{SFR}. \quad (20)$$

Below, we discuss each quantity in equation (20).

(i) L_{Edd} , the Eddington luminosity, which scales with the typical mass of the BH engine M_{BH} as $1.3 \times 10^{38} (M_{\text{BH}} / \text{M}_{\odot}) \text{ erg s}^{-1}$.

(ii) f_{Edd} , the typical ratio of the total radiative power emitted by HMXBs (the bolometric luminosity) to L_{Edd} . If the typical luminosity of a HMXB during an active phase is Eddington, then f_{Edd} is effectively the mean duty cycle. Other studies have adopted values ranging from 0.1 to 0.5 (Mirabel et al. 2011; Belczynski et al. 2008; Salvaterra et al. 2012b); we take as our fiducial value $f_{\text{Edd}} = 0.1$.

(iii) $f_{2-10 \text{ keV}}$, the fraction of the bolometric luminosity that is emitted between 2 and 10 keV. Observational estimates vary between 0.1 and 0.8 (e.g. Sipior, Eracleous & Sigurdsson 2003; Migliari & Fender 2006). Because the BH masses in Pop III HMXBs are expected to be higher than in present-day populations, and the peak energies of accretion disks scale with the mass of the central engine as $M_{\text{BH}}^{-1/4}$, their characteristic spectra could be somewhat softer. We do not expect this to significantly affect our estimates here.

(iv) t_{acc} , the time that a massive binary spends as a HMXB, with the less massive star donating mass to the more massive BH companion. If the two stars form simultaneously and form a compact binary before the more massive member dies to become a BH, then this is simply $t_2 - t_1$, the difference in the lifetimes of the stars. We use this (somewhat arbitrary) estimate. However, because the lifetimes of the less massive star ($t_2 \gtrsim 10 \text{ Myr}$ for stars with masses $\lesssim 10 \text{ M}_{\odot}$) are comparable to the expected specific star formation rate in galaxies at this redshift, we argue that any prescription that satisfies $t_{\text{acc}} \lesssim t_2$ is a reasonable order-of-magnitude estimate.

(v) f_{sur} , the fraction of HMXB candidates identified in

our simulations that actually survive to become HMXBs. This quantity accounts for possible disruptions of binaries, due to (a) the merger of the stars during main sequence and post-main sequence evolution (Power et al. 2009); (b) the more massive star getting kicked following a supernova explosion (e.g. Repetto, Davies & Sigurdsson 2012; Janka 2013); and (c) subsequent disruptions by stellar scatterings that were not captured by our simulations. (Our simulations follow the evolution of star groups until the formation of a stable compact binary, but not until stellar death millions of years later.) Theoretical estimates typically yield $\sim 0.2 - 0.3$ (e.g. Jeon et al. 2014; Artale, Tissera & Pellizza 2015).

(vi) f_{esc} , the fraction of X-rays that escape the galaxy. Unless the environment of the HMXBs are Compton-thick, which is unlikely for the low-mass galaxies of interest, we expect $f_{\text{esc}} \lesssim 1$.

(vii) F_{HMXB} , the number of HMXBs formed per stellar mass. This is the main output of our simulations. Whereas previous theoretical works had arrived at this value by extrapolating the locally observed value with an assumed redshift evolution, or with free parameters, here we provide an estimate based on suites of N -body simulations whose initial conditions are motivated by cosmological simulations of Pop III star formation. (Note that this quantity has units M_{\odot}^{-1} ; we use the capital letter to distinguish it from the dimensionless fractions represented by f)

Across all of our small-scale simulations—varying the number of stars in the group, whether groups evolved in isolation or through several different orientations of mutual collisions, and exploring two values for the ambient gas density separated by two orders of magnitude—we find $F_{\text{HMXB}} \sim 10^{-3}$, varying by less than a factor of 4 between the lowest and the highest values (see Table 4).

Finally, we can write $L_{2-10 \text{ keV}}$ as follows :

$$\begin{aligned} \frac{L_{2-10 \text{ keV}}}{\text{SFR}} &= 0.33 \times \frac{M_{\text{BH}}}{\text{M}_{\odot}} \times \frac{f_{\text{Edd}}}{0.1} \times \frac{f_{2-10 \text{ keV}}}{0.1} \times \frac{t_{\text{acc}}}{\text{Myr}} \\ &\times \frac{f_{\text{sur}}}{0.5} \times \frac{f_{\text{esc}}}{0.5} \times \frac{F_{\text{HMXB}}}{10^{-3} \text{ M}_{\odot}^{-1}} \\ &\times \frac{10^{39} \text{ erg s}^{-1}}{\text{M}_{\odot} \text{ yr}^{-1}}. \end{aligned} \quad (21)$$

Based on our choices of the factors, $f_{\text{Edd}} = 0.1$, $f_{2-10 \text{ keV}} = 0.1$, $f_{\text{sur}} = 0.5$ and $f_{\text{esc}} = 0.5$, we can estimate the normalized X-ray luminosities per SFR, $L_{2-10 \text{ keV}} / \text{SFR}$. We report this quantity for each of our models in Table 4. It varies from a minimum of 37 to a maximum of 450 among the studied scenarios.

These L_X -to-SFR ratios are $\sim 40 - 150$ higher than what is observed in the local Universe. This result is qualitatively consistent with the findings of Basu-Zych et al. (2013) and Kaaret (2014), who find an increase in the L_X -to-SFR ratios toward $z \gtrsim 4$. Our high L_X -to-SFR values stem from the large mass of the HMXBc primary, and the relatively low mass of the secondary. The former leads to a higher Eddington luminosity compared to typical stellar-mass BHs ($\sim 3 \text{ M}_{\odot}$) in the local Universe, and the latter results in long stellar lifetimes, which in turn leads to longer t_{acc} . Note that we used the stellar mass as a proxy for the BH mass for simplicity, due to the theoretical uncertainties in evaluating the mass loss due to winds and during the transition to a

BH. Any significant mass loss (e.g. simulations by Zhang, Woosley & Heger 2008 suggest that the BH remnants of massive metal-free stars end up with $\sim 40\%$ of the progenitor mass) would be directly translatable to the estimated X-ray luminosities reported in Table 4.

4.4 Implications for the thermal history of the IGM and the 21cm radiation

A higher L_X -to-SFR ratio implies that IGM heating will occur earlier than commonly thought. The thermal history of the IGM can be probed in the 21 cm line, which is observable in absorption (or in emission), depending on whether the spin temperature of the IGM is below (or above) the CMB temperature.

If the IGM heats early, as suggested by our estimates of the X-ray emission of early galaxies, the 21 cm absorption line appears earlier, and the “dip” as a function of redshift caused by adiabatic cooling is not as deep and not as sharp as in the case of late heating as it would otherwise (see Figure 2 in Fialkov & Barkana 2014). Another consequence of early, intense heating is that the temperature of the IGM could become high enough, to suppress the formation of low-mass galaxies (Ripamonti, Mapelli & Zaroubi 2008) and the growth of their nuclear BHs (Tanaka, Perna & Haiman 2012).

4.5 Implications for Gamma Ray Bursts from Pop III stars

As discussed in §1, the fraction of HMXBs at high redshifts has potential implications for the expected rates of LGRBs from Pop III stars. According to the collapsar model (MacFadyen & Woosley 1999), for an exploding massive star to yield a GRB, several conditions need to be satisfied, namely:

- (i) The core of the star must collapse to a BH. This is realized by most Pop III stars, given their large masses.
- (ii) The hydrogen envelope of the progenitor star must be stripped, so that a relativistic jet can penetrate and exit the remaining envelope.
- (iii) The BH should be surrounded by an accretion disk of high angular momentum material. This is realized if the core of the progenitor star has retained sufficient angular momentum during the evolution.

Binary systems more easily satisfy the last two conditions with respect to single stars (see e.g. Cantiello et al. 2007). In fact, for single stars to end their lives as LGRBs, they need to be born with large initial rotation (since they are less likely to be spun up by other stars), and also avoid being slowed down by magnetic torques (e.g. Spruit 2002; Yoon, Langer & Norman 2006; Perna et al. 2014).

In contrast, binary stars can spin up the helium core of the progenitor star via tidal coupling and spin-orbit locking. Further, RLOF can strip the hydrogen envelope during a common-envelope phase without reducing the rotation of the helium core (Bromm & Loeb 2006). This is especially important for Pop III stars, whose heavier hydrogen envelopes would be more difficult to shed in isolation. Therefore, compact binary systems, or HMXBs, constitute a promising channel to produce LGRBs from Pop III stars.

We can use our results for the formation rates of Pop III HMXBs to estimate the fraction of LGRBs from Pop III stars¹. Bromm & Loeb (2006) quantified the GRB formation efficiency as

$$\eta_{\text{GRB}} \simeq \eta_{\text{BH}} \eta_{\text{bin}} \eta_{\text{close}} \eta_{\text{beaming}}, \quad (22)$$

where η_{BH} is the number of BH-forming stars resulting from a given total stellar mass, η_{bin} is the binary fraction and η_{close} is the fraction of sufficiently close binaries to undergo RLOF. For Pop I/II stars they calculated $\eta_{\text{BH}} \simeq 1/(700 M_{\odot})$. Combining this value with adopted values for the other parameters— $\eta_{\text{bin}} \sim 0.5$, $\eta_{\text{close}} \sim 0.3$, and $\eta_{\text{beaming}} \simeq (1/50) - (1/500)$ —yields $\eta_{\text{GRB,Pop I/II}} \sim 4.2 \times (10^{-6} - 10^{-7}) M_{\odot}^{-1}$.

Bromm & Loeb (2006) noted that it was only to make educated guesses for the Pop III case, due to an absence of detailed calculations for the fraction of close binaries. Our work is a first attempt to fill the gap in our theoretical knowledge. We can write $F_{\text{HMXB}} = \eta_{\text{BH}} \eta_{\text{bin}} \eta_{\text{close}}$. Adopting for comparison the same value of $\eta_{\text{beaming}} \simeq (1/50) - (1/500)$, we then infer $\eta_{\text{GRB,Pop III}} \simeq 4.8 \times (10^{-6} \sim 10^{-7}) M_{\odot}^{-1}$ for the interacting 5-star case, and $2.2 \times (10^{-5} \sim 10^{-6}) M_{\odot}^{-1}$ for the (most favorable) 10-body scenario.

Therefore, our results suggest that LGRB rates from Pop III stars could be comparable to or somewhat higher than the rates from Pop I/II stars.

4.6 Caveats

Our suite of N -body simulations, spanning diverse sets of initial conditions for Pop III stars and their environments, point that HMXBs form in higher fractions in the earliest galaxies than at low redshifts, and make significant contributions to the thermal history of the IGM, the 21 cm signature at $z \sim 20$, and to the rates of LGRBs. The fact that the formation rates of HMXBs varied little between the simulations suggest that our estimates for F_{HMXB} is reasonably robust. However, we here point out several uncertainties of our work that could affect our conclusions.

One important factor is the IMF of the stars (e.g. Hirano et al. 2014). We adopted the IMF of Stacy & Bromm (2013), which were based on the masses of protostars roughly 5000 yr after the formation of the protostellar seeds.

However, our key results are based on fragmentation of the protostellar clouds on smaller scales, as found in the simulations by Greif et al. (2011). In those simulations, the most massive protostars had the highest accretion rates, suggesting that the IMF slope may be steeper than what we assumed. We also did not account for changes in the masses of stars as they evolved. These are important considerations,

¹ Note that in our study, since we are considering HMXB ‘candidates’, there is also the possibility of merger of the two stars during the common-envelope inspiral phase, when they both are stripped down to their Helium cores. This event could provide another avenue for the formation of GRBs (Fryer & Heger 2005). Alternatively, after both stars have undergone the SN explosion, if the system is still bound, the compact objects of the binary, upon merger as a result of gravitational energy loss, would be likely contributors to the population of Short Gamma-Ray Bursts (e.g. Narayan, Paczynski & Piran 1992).

	5-body(n_6)	5-body(n_4)	<i>Sce. 1</i>	<i>Sce. 2</i>	<i>Sce. 3</i>	<i>Sce. 4A</i>	<i>Sce. 4B</i>
$M_1 [M_\odot] (\tau_{\text{life},1} [\text{Myr}])$	110(2.5)	88(2.9)	110(2.5)	120(2.4)	110(2.4)	160(2.0)	110(2.4)
$M_2 [M_\odot] (\tau_{\text{life},2} [\text{Myr}])$	12(17)	11(18)	18(11)	45(4.8)	28(7.1)	63(3.7)	63 (3.7)
$t_{\text{acc}} (= \tau_{\text{life},2} - \tau_{\text{life},1}) [\text{Myr}]$	14	15	8.6	2.5	4.7	1.7	1.3
$F_{\text{HMXB}} [10^{-4} M_\odot^{-1}]$	4.6	4.6	15	11	9.0	4.2	8.4
$L_{2-10\text{keV}}/\text{SFR} [10^{39} \text{ergs}^{-1} M_\odot^{-1} \text{yr}]$	220	200	450	107	160	37	40
$L_{2-10\text{keV}}/L_{2-10\text{keV}}^{\text{local}}$	75	67	150	36	52	12	13
$\frac{\eta_{\text{GRB,PopIII}}}{\eta_{\text{GRB,PopI/II}}}$	2.2	2.2	7.0	5.4	4.3	2.0	4.0

Table 4. Summary of the results of X-ray luminosity and GRB efficiencies. In the table, second and third columns correspond to 5-body calculations and the rest columns (from *Sce. 1* to *Sce. 4B*) are the results from 10-body calculations with the number density of 10^6cm^{-3} . According to the ratio $L_{2-10 \text{ keV}}/L_{2-10 \text{ keV}}^{\text{local}}$, where $L_{2-10 \text{ keV}}^{\text{local}} = 3 \times 10^{39} \text{ erg s}^{-1}$, it is expected that the 2-10 keV X-ray luminosity is $\sim 10^2$ times larger than the X-ray luminosity of the local universe. These larger values essentially result from the large mass of the star 1. In the bottom row, we have listed the LGRB efficiency, derived from each set of simulations. The higher HMXB formation rates, lead to larger efficiencies than the estimated value for Pop I/II stars, $\eta_{\text{GRB,PopI/II}} \simeq 4.2 \times 10^{-6}$ with beaming factor of 1/50 (e.g. Bromm & Loeb 2006).

as the masses of the stars play a critical role in determining the time that a binary spends transferring mass as a HMXB.

We made an effort to account for this limitation by using free parameters such as f_{sur} , which accounts for the mass loss during the SN explosion.

Another factor that could be more carefully treated in future studies is the spin of the star. In a binary system, this impacts the circularization of the orbit, followed by low eccentricity and the synchronization of spin with orbital phase.² Due to tidal dissipation and circularization, this could additionally decrease the orbital distance of a binary, boosting the formation of HMXBs and change the average value of the eccentricity.

In addition to reducing the orbital separation, the spin makes a difference in mass transfer rates.

Our simulations generally produce binaries with large eccentricities. For highly eccentric orbits, mass transfer occurs only near pericenter (Lajoie & Sills 2011 and Sepinsky et al. 2010), and the rates depend on whether the orbital angular speed of the star is super-synchronous or sub-synchronous with rotational angular speed (Davis, Siess & Deschamps 2013).

We found that the viscous timescales in our eccentric binaries were longer than the orbital timescales in the majority of cases, and used this fact to conclude that their duty cycle should be the same as for nearly circular binaries. However, we did find one exception, in which a RLOF accretion event would be sufficiently short-lived to be episodic. A more careful study focused on stellar rotation effects may be necessary to more conclusively estimate the duty cycle of eccentric Pop III HMXBs.

Finally, our simulations are an attempt to model the stellar dynamics as a gravitational N -body problem with perturbative forces due to a fixed, smooth gaseous background. More detailed simulations that include detailed stellar feedback, as well as the dynamics and thermodynamics

of the gaseous environment, could lead to additional revelations about the early evolution of Pop III star groups.

5 SUMMARY

In this study, we used N -body simulations of the first stars to explore the formation, evolution, disruption and energy output of Pop III HMXBs. The code includes gravitational scattering of stars, dynamical friction, and the gravitational potential of ambient gas.

The initial conditions for the simulations (i.e. IMF, typical star separation in the host haloes, ambient densities) are taken from two different sets of cosmological simulations of Pop III formation, namely by Stacy & Bromm (2013) ('large-scale', i.e. a few thousands of AU), and Greif et al. (2012), ('small-scale', i.e. a few tens of AU). These provide two complementary sets in that they explore different physical scales for star formation (for details, see 2.4). For each of the two scenarios, we investigated star evolution in two background gas densities, a high-density case (10^6cm^{-3}), and a lower-density one (10^4cm^{-3}).

Based on the handful of protostars per halo that are found in the works quoted above, we simulated systems with 5 stars and systems with 10 stars. We found:

(i) *5-body simulations*: If stars form in quasi-Keplerian disk configurations with initial separations of hundreds of AU, HMXBs are highly unlikely to form. In contrast, if stars form in compact groups separated by ~ 10 AU, as is expected from turbulent fragmentation, stellar scatterings lead to a significant HMXB formation rate. In particular, we found that HMXBs form at a rate of a few per $10^4 M_\odot$ of stars formed, independent of the ambient gas density.

(ii) *10-body simulations*: We simulated 10 stars on separations of ~ 10 AU, and evolved them as isolated quasi-Keplerian disks, or as two colliding groups with 5 stars each. For the latter, we ran several different sets of collision geometries.

We found that the HMXB formation rate was a factor $\sim 1-3$ times higher than for the 5-body simulations, mainly due to the fact that the larger number of stars allowed for more hardening via stellar scattering.

All of the small-scale simulations suggest an X-ray lumi-

² These effects had been often assumed to be due to the tidal interactions with accreting gas, but recent studies suggest that the orbital semimajor axis and eccentricity can either increase or decrease depending on the binary properties at pericenter (Sepinsky, Willems & Kalogera 2007 and Sepinsky et al. 2009).

osity per unit star formation that is a factor $\sim 10^2$ higher than what is observed in the local Universe (under the assumption that other variables such as the X-ray escape fraction from galaxies and the duty cycle of HMXBs do not differ significantly). These results are mostly due to *the large mass of the most massive star of the HMXBc compared to that of the companion star, implying both a large t_{acc} as well as a higher luminosity of the remnant BH*. The fact that we found little variation in this quantity across all of our simulations suggests that this is a robust estimate. Additional factors, such as in-disk migration of nascent stars, could further increase the HMXB formation efficiency.

A direct consequence is that X-rays can heat the IGM rapidly at Cosmic Dawn. Signals of early heating can be probed via the 21 cm line radiation: the absorption line signal is expected to show a broader, shallower minimum due to the shorter gas cooling time, while the emission line would be observed earlier because of the higher gas temperature, at earlier times. Several studies have modeled the 21 cm signature of the first HMXBs, but relied on assumptions for their L_X/SFR relation relative to the empirical value found at lower redshifts. Our work provides a theoretically driven estimate for this quantity.

In addition to the implications for the thermal history of the IGM, these high formation rates of HMXBs per stellar mass imply a higher GRB formation efficiency from Pop III stars in binaries. This predictions can be tested with a long baseline of observational data from *Swift*.

Acknowledgements We are grateful to Zoltán Haiman and Mark Dijkstra for meaningful comments and suggestions which helped to improve this work.

REFERENCES

- Abel T., Bryan G. L., Norman M. L., 2002, *Science*, 295, 93
- Artale M. C., Tissera P. B., Pellizza L. J., 2015, *M.N.R.A.S.*, 448, 3071
- Bañados E. et al., 2014, *AJ*, 148, 14
- Basu-Zych A. R. et al., 2013, *ApJ*, 762, 45
- Belczynski K., Kalogera V., Rasio F. A., Taam R. E., Zezas A., Bulik T., Maccarone T. J., Ivanova N., 2008, *ApJ Supp.*, 174, 223
- Binney J., Tremaine S., 1987, *Galactic dynamics*
- Bowman J. D., Rogers A. E. E., Hewitt J. N., 2008, *ApJ*, 676, 1
- Bromm V., Loeb A., 2006, *ApJ*, 642, 382
- Bromm V., Yoshida N., 2011, *Ann. Rev. A&A*, 49, 373
- Burns J. O. et al., 2012, *Advances in Space Research*, 49, 433
- Cantiello M., Yoon S.-C., Langer N., Livio M., 2007, *A&A*, 465, L29
- Davis P. J., Siess L., Deschamps R., 2013, *A&A*, 556, A4
- Dijkstra M., Gilfanov M., Loeb A., Sunyaev R., 2012, *M.N.R.A.S.*, 421, 213
- Eggleton P. P., 1983, *ApJ*, 268, 368
- Erwin F., 1969, *NASA Technical Report*, 315, 1
- Escala A., Larson R. B., Coppi P. S., Mardones D., 2004, *ApJ*, 607, 765
- Fan X. et al., 2001, *AJ*, 122, 2833
- Fialkov A., Barkana R., 2014, *M.N.R.A.S.*, 445, 213
- Fialkov A., Barkana R., Visbal E., 2014, *Nat.*, 506, 197
- Frank J., King A., Raine D. J., 2002, *Accretion Power in Astrophysics: Third Edition*
- Fryer C. L., Heger A., 2005, *ApJ*, 623, 302
- Furlanetto S. R., 2006, *M.N.R.A.S.*, 371, 867
- Gilfanov M., Grimm H.-J., Sunyaev R., 2004, *M.N.R.A.S.*, 347, L57
- Gnedin N. Y., 2000, *ApJ*, 542, 535
- Greif T. H., Bromm V., Clark P. C., Glover S. C. O., Smith R. J., Klessen R. S., Yoshida N., Springel V., 2012, *M.N.R.A.S.*, 424, 399
- Greif T. H., Springel V., White S. D. M., Glover S. C. O., Clark P. C., Smith R. J., Klessen R. S., Bromm V., 2011, *ApJ*, 737, 75
- Grimm H.-J., Gilfanov M., Sunyaev R., 2003, *M.N.R.A.S.*, 339, 793
- Haiman Z., 2013, in *Astrophysics and Space Science Library*, Vol. 396, *Astrophysics and Space Science Library*, Wiklund T., Mobasher B., Bromm V., eds., p. 293
- Haiman Z., Rees M. J., Loeb A., 1996, *ApJ*, 467, 522
- Heger A., Fryer C. L., Woosley S. E., Langer N., Hartmann D. H., 2003, *ApJ*, 591, 288
- Hinshaw G. et al., 2013, *ApJ Supp.*, 208, 19
- Hirano S., Hosokawa T., Yoshida N., Umeda H., Omukai K., Chiaki G., Yorke H. W., 2014, *ApJ*, 781, 60
- Hopkins P. F., Quataert E., 2010, *M.N.R.A.S.*, 407, 1529
- Inayoshi K., Tanaka T. L., 2015, *M.N.R.A.S.*, 450, 4350
- Janka H.-T., 2013, *M.N.R.A.S.*, 434, 1355
- Jeon M., Pawlik A. H., Bromm V., Milosavljević M., 2014, *M.N.R.A.S.*, 440, 3778
- Kaaret P., 2014, *M.N.R.A.S.*, 440, L26
- Kozai Y., 1962, *AJ*, 67, 591
- Kuhlen M., Madau P., 2005, *M.N.R.A.S.*, 363, 1069
- Lajoie C.-P., Sills A., 2011, *ApJ*, 726, 67
- Latif M. A., Bovino S., Grassi T., Schleicher D. R. G., Spaans M., 2015, *M.N.R.A.S.*, 446, 3163
- Lubow S. H., Ida S., 2010, *Planet Migration*, Seager S., ed., pp. 347–371
- MacFadyen A. I., Woosley S. E., 1999, *ApJ*, 524, 262
- Machacek M. E., Bryan G. L., Abel T., 2003, *M.N.R.A.S.*, 338, 273
- Madau P., Haardt F., Dotti M., 2014, *ApJL*, 784, L38
- Marigo P., Chiosi C., Kudritzki R.-P., 2003, *A&A*, 399, 617
- McGreer I. D., Becker R. H., Helfand D. J., White R. L., 2006, *ApJ*, 652, 157
- Migliari S., Fender R. P., 2006, *M.N.R.A.S.*, 366, 79
- Mineo S., Gilfanov M., Sunyaev R., 2012, *M.N.R.A.S.*, 419, 2095
- Mirabel I. F., Dijkstra M., Laurent P., Loeb A., Pritchard J. R., 2011, *A&A*, 528, A149
- Mortlock D. J. et al., 2011, *Nat.*, 474, 616
- Naoz S., Barkana R., 2007, *M.N.R.A.S.*, 377, 667
- Narayan R., Paczynski B., Piran T., 1992, *ApJL*, 395, L83
- Oh S. P., 2001, *ApJ*, 553, 499
- Ostriker E. C., 1999, *ApJ*, 513, 252
- Pacucci F., Ferrara A., Volonteri M., Dubus G., 2015, *ArXiv e-prints*
- Perna R., Duffell P., Cantiello M., MacFadyen A. I., 2014, *ApJ*, 781, 119
- Persic M., Rephaeli Y., Braitto V., Cappi M., Della Ceca R., Franceschini A., Gruber D. E., 2004, *A&A*, 419, 849

- Planck Collaboration et al., 2015, ArXiv e-prints
- Power C., Wynn G. A., Combet C., Wilkinson M. I., 2009, M.N.R.A.S., 395, 1146
- Pritchard J. R., Furlanetto S. R., 2007, M.N.R.A.S., 376, 1680
- Pritchard J. R., Loeb A., 2008, *prd*, 78, 103511
- Regös E., Bailey V. C., Mardling R., 2005, M.N.R.A.S., 358, 544
- Repetto S., Davies M. B., Sigurdsson S., 2012, M.N.R.A.S., 425, 2799
- Ricotti M., Ostriker J. P., 2004, M.N.R.A.S., 352, 547
- Ripamonti E., Mapelli M., Zaroubi S., 2008, M.N.R.A.S., 387, 158
- Salvaterra R., Haardt F., Volonteri M., Moretti A., 2012a, A&A, 545, L6
- Salvaterra R., Haardt F., Volonteri M., Moretti A., 2012b, A&A, 545, L6
- Schaerer D., 2002, in *Astrophysics and Space Science Library*, Vol. 274, *New Quests in Stellar Astrophysics: the Link Between Stars and Cosmology*, Chávez M., Bressan A., Buzzoni A., Mayya D., eds., pp. 185–188
- Seager S., 2010, *Exoplanets*
- Sepinsky J. F., Willems B., Kalogera V., 2007, ApJ, 660, 1624
- Sepinsky J. F., Willems B., Kalogera V., Rasio F. A., 2009, ApJ, 702, 1387
- Sepinsky J. F., Willems B., Kalogera V., Rasio F. A., 2010, ApJ, 724, 546
- Shakura N. I., Sunyaev R. A., 1973, A&A, 24, 337
- Shankar F., Weinberg D. H., Miralda-Escudé J., 2009, ApJ, 690, 20
- Shen Y. et al., 2007, AJ, 133, 2222
- Sijacki D., Springel V., Di Matteo T., Hernquist L., 2007, M.N.R.A.S., 380, 877
- Sipior M. S., Eracleous M., Sigurdsson S., 2003, ArXiv Astrophysics e-prints
- Springel V., Di Matteo T., Hernquist L., 2005, M.N.R.A.S., 361, 776
- Spruit H. C., 2002, A&A, 381, 923
- Stacy A., Bromm V., 2013, M.N.R.A.S., 433, 1094
- Stacy A., Greif T. H., Bromm V., 2010, M.N.R.A.S., 403, 45
- Stinson G., Seth A., Katz N., Wadsley J., Governato F., Quinn T., 2006, M.N.R.A.S., 373, 1074
- Syer D., Clarke C. J., 1995, M.N.R.A.S., 277, 758
- Tan J. C., Blackman E. G., 2004, ApJ, 603, 401
- Tan J. C., McKee C. F., 2004, ApJ, 603, 383
- Tanaka T., Haiman Z., 2009, ApJ, 696, 1798
- Tanaka T., O’Leary R., Perna R., 2015, M.N.R.A.S. submitted
- Tanaka T., Perna R., Haiman Z., 2012, M.N.R.A.S., 425, 2974
- Tanaka T. L., 2014, *Classical and Quantum Gravity*, 31, 244005
- Tanaka T. L., Li M., 2014, M.N.R.A.S., 439, 1092
- Toma K., Sakamoto T., Mészáros P., 2011, ApJ, 731, 127
- Treister E., Schawinski K., Urry C. M., Simmons B. D., 2012, ApJL, 758, L39
- Turk M. J., Abel T., O’Shea B., 2009, *Science*, 325, 601
- van Haarlem M. P. et al., 2013, A&A, 556, A2
- Venemans B. P. et al., 2013, ApJ, 779, 24
- Venkatesan A., Giroux M. L., Shull J. M., 2001, ApJ, 563, 1
- Venkatesan A., Tumlinson J., Shull J. M., 2003, ApJ, 584, 621
- Volonteri M., 2010, A&A Rev., 18, 279
- Voytek T. C., Natarajan A., Jáuregui García J. M., Peterson J. B., López-Cruz O., 2014, ApJL, 782, L9
- Willott C. J. et al., 2007, AJ, 134, 2435
- Willott C. J. et al., 2009, AJ, 137, 3541
- Yoon S.-C., Langer N., Norman C., 2006, A&A, 460, 199
- Zhang W., Woosley S. E., Heger A., 2008, ApJ, 679, 639